

Chiral geometry driven chiral magnetism

Yonglong Ga,^{1,*} Dongxing Yu^{2,*} Jiawei Jiang,¹ Liming Wang,¹ Fengjun Zhuo^{1,†} Kai Chang,^{1,‡} and Hongxin Yang^{1,§}

¹Center for Quantum Matter, School of Physics, Zhejiang University, Hangzhou 310058, China

²Key Laboratory of Magnetism and Magnetic Functional Materials of MoE, Lanzhou University, Lanzhou 730000, China



(Received 30 September 2025; revised 2 December 2025; accepted 4 December 2025; published 5 January 2026)

We extend the study of topological magnetisms to quasi-one-dimensional chiral geometries, revealing a symmetry-guided pathway to Dzyaloshinskii–Moriya interactions (DMI) and enabling the design of high-density spintronic devices. Utilizing symmetry analysis, a general strategy is proposed for inducing Bloch-type DMI in chiral geometries warped by low-dimensional magnets. By combining first-principles calculations, we demonstrate our concept in various chiral geometries, e.g., chiral nanoribbon and nanotubes, which are composed of quasi-one-dimensional CrBr₂ nanoribbon and two-dimensional magnets with different crystal symmetries, including CrN, transition metal dichalcogenides, VSe, CrI₃, and Cr₂Se₃. More interestingly, we find that the chirality of Bloch-type DMI can be closely coupled with the helical direction of the chiral geometry. Our atomistic spin dynamics study using Monte Carlo simulation is performed on chiral VS₂ nanotube as an example, in which Bloch-type domain walls with opposite chirality arising from Bloch-type DMI can be stabilized via opposite chirality indices (n, m) and (m, n). Our results that chiral geometry induces DMI in a broad range of 2D magnets, enabling topological magnetisms, pave the way for the development of geometry-driven spintronic devices.

DOI: 10.1103/81rn-9t23

I. INTRODUCTION

Dzyaloshinskii–Moriya interaction (DMI) [1,2], as a counterpart of Heisenberg exchange coupling, has emerged as a key magnetic parameter in determining the ground state of magnetic systems, such as chiral domain wall (DW) [3,4], spin spirals [5], magnetic skyrmions [6–8] and bimerons [9,10]. Depending on the crystal symmetry, three distinct types of DMI have been reported, namely, interfacial (Néel-type), bulk (Bloch-type), and anisotropic DMI. The DMI energy density (w_{DM}) can be expressed as a combination of so-called Lifshitz invariants: $\mathcal{L}_{ij}^{(k)} = m_i \partial_k m_j - m_j \partial_k m_i$ according to crystallographic point-group symmetry [11–13], where i , j , and k are an arbitrary choice of Cartesian coordinates x , y , and z . Thereby, the former can be identified as $w_{\text{DM}} = D[\mathcal{L}_{xz}^{(x)} + \mathcal{L}_{yz}^{(y)}]$, which usually exists in interfacial system with C_{nv} symmetry, e.g., ferromagnetic (FM)/heavy metal, FM/oxides multilayers [14–21]. Bulk DMI energy term can be written as $w_{\text{DM}} = D[\mathcal{L}_{yx}^{(z)} + \mathcal{L}_{xz}^{(y)} + \mathcal{L}_{yz}^{(x)}]$, where such form has been found in bulk materials with T or O symmetry, e.g., noncentrosymmetric B20 magnets [7,8,13,22]. For the lastest, the DMI energy is given as $w_{\text{DM}} = D[\mathcal{L}_{xz}^{(y)} + \mathcal{L}_{yz}^{(x)}]$ or $w_{\text{DM}} = D[\mathcal{L}_{xz}^{(x)} - \mathcal{L}_{yz}^{(y)}] + D'[\mathcal{L}_{xz}^{(y)} + \mathcal{L}_{yz}^{(x)}]$, which is reported in D_{2d} or S_4 symmetry [23–26]. Based on above particular forms, Néel-, Bloch-type, and anisotropic magnetic textures can be quantitatively distinguished by helicity angles according to magnetization vector of ground state. In parallel with

the development of intensive studies of DMI in traditional bulk and interfacial thin films, the experimental breakthrough in two-dimensional (2D) magnets in recent years has stimulated the exploration of the possibility of intrinsic DMI in this new material platform because of its atomic thickness, flexible designability, and tunable electronic properties [27–29]. However, the reported 2D magnets are generally centrosymmetric, and such a geometric characteristic betrays the principle underlying the DMI generation. Attractively, a variety of effective strategies have been proposed to obtain sizable DMI and chiral spin textures, such as Janus magnets [30,31], intercalation [32,33], intrinsic multiferroic or ferromagnet-based heterostructures [34–37], twist magnets [38–40], and curvature-induced structures [41]. These efforts highlight the progress in engineering DMI in bulk, interfacial, and 2D systems; however, the potential of quasi-one-dimensional chiral geometries for hosting intrinsic DMI and topological spin textures remains largely unexplored.

In this paper, combining symmetry analysis and numerical calculations, we propose a strategy to generate Bloch-type DMI in low-dimensional magnets driven by chiral geometry. Chiral geometry, rolled-up from low-dimensional flat counterparts, exhibits fascinating features and has spurred extensive researches in various fields of physics [42–48]. More recently, experimental works have revealed chirality-controlled synthesis and preparation of chiral geometry inspire us to investigate the chirality-dependent magnetic properties in such systems [49–57]. From the reported materials databases [58,59], we select a series of low-dimensional magnets with different crystal symmetries, including quasi-one-dimensional CrBr₂, 2D hexagonal chromium nitride (CrN), transition metal dichalcogenides (TMDs), tetragonal VSe and trigonal CrI₃, Cr₂Se₃ [60–64]. By means of the qSO method [65,66],

*These authors contributed equally to this work.

†Contact author: kchang@zju.edu.cn

‡Contact author: hongxin.yang@zju.edu.cn

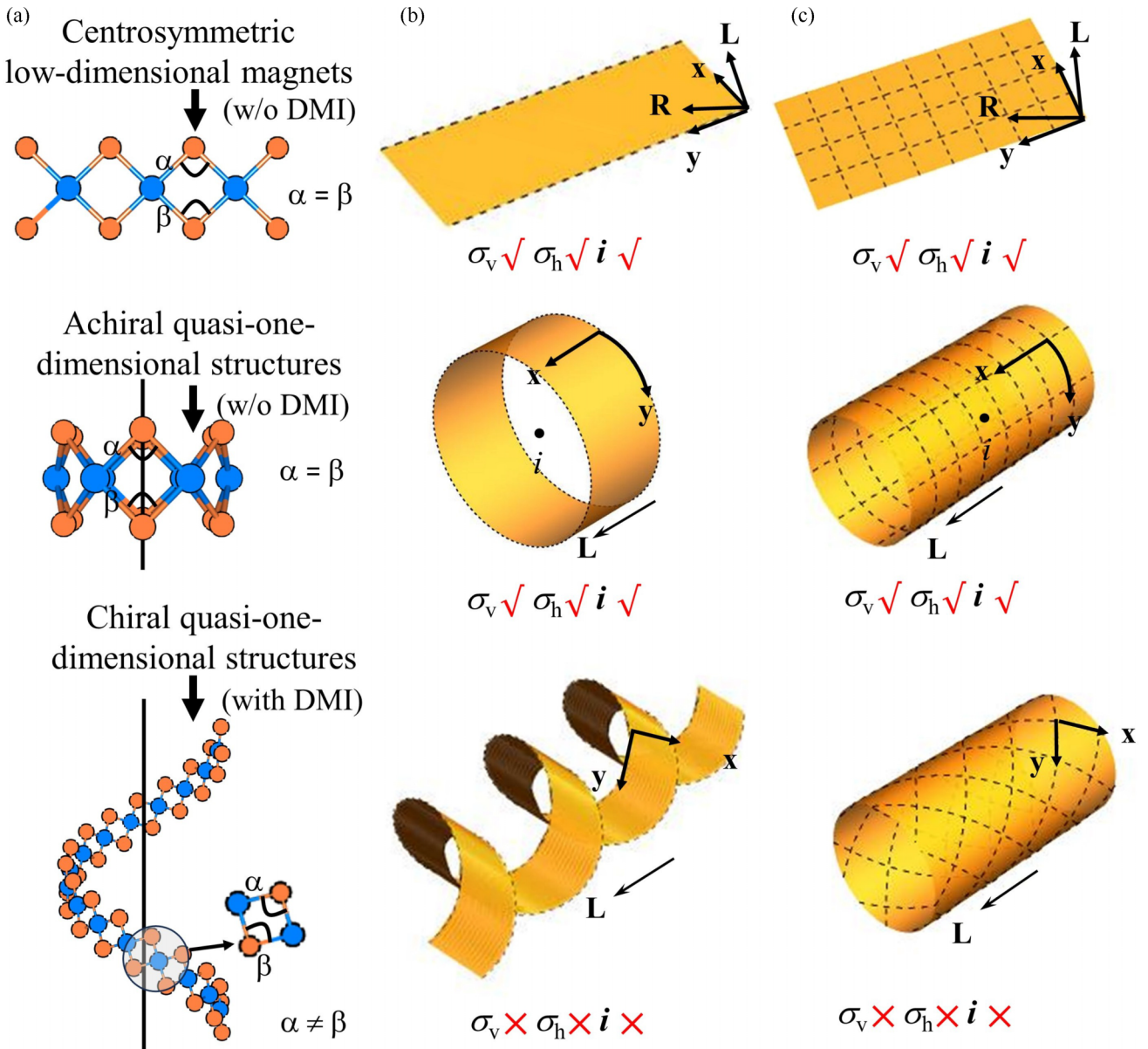


FIG. 1. (a) Schematic low-dimensional, achiral and chiral nanoribbons, where inversion center i be broken in the chiral structures, resulting in inherent DMI parameters. α and β are the bond angles of each $M-X-M$ trimer, where M and X represent the magnetic and nonmagnetic atoms, respectively. (b) Wrapped nanoring and chiral nanoribbon along the y and chiral vector \mathbf{R} directions in quasi-one-dimensional nanoribbon. (c) Achiral and chiral nanotubes are formed via rolling up planer structure along chiral vector \mathbf{R} direction. Here, σ_v , σ_h , and i represent the symmetry operations of vertical mirror, horizontal mirror, and inversion symmetry center.

we systematically investigate their chiral geometry-driven DMI effects. We reveal that Bloch-type DMI is preserved in quasi-one-dimensional chiral nanoribbon and chiral nanotubes, while Néel-type DMI disappears completely. In addition, we find that the chirality of DMI and noncollinear spin textures is closely coupled with helical directions of chiral geometry. Our Monte Carlo simulations reveal that Bloch-type DW with opposite chirality arising from Bloch-type DMI can also be stabilized in chiral (6, 3) and (3, 6) VS₂ nanotubes. Our findings indicate that designing chiral geometry is a plausible approach to inducing Bloch-type DMI and topological magnetism in quasi-one-dimensional magnets.

II. MODEL DESIGN AND SYMMETRY ANALYSIS

When a planar 2D magnet is rolled into chiral geometry along a given direction, inversion center (i) is spontaneously broken, resulting in intrinsic DMI, as schematically shown in Fig. 1(a). For convenience, we initially consider a ferromagnetic nanoribbon with i characterized by edge orientation (y) and finite width of ribbon (x) [Fig. 1(b)]. To induce DMI, we design the quasi-one-dimensional nanoribbon along \mathbf{R} to construct the helical geometry based on following transformation: $\begin{pmatrix} x \\ y \\ z \end{pmatrix} \rightarrow \begin{pmatrix} x(s) \\ y(s) \\ z(s) \end{pmatrix}$, where $x(s) = r \cos(ks)$, $y(s) = r \sin(ks)$, $z(s) = ps$. Here, s is the arc-length parameter, r denotes the radius of the chiral nanoribbon; $k = 1/r$ ensures

that a full 2π rotation corresponds to an increase in s of $2\pi r$, and p is the pitch per unit arc length. \mathbf{R} represents the chiral vector between x and y axis and \mathbf{L} is the vector perpendicular to \mathbf{R} and parallel to the axis of helical nanoribbon. Then, we obtain the following two helical nanoribbons: nanoring wrapped from x directions with inherent i ; chiral nanoribbon with inherent inversion asymmetry, whose DMI tensor can be identified as $\begin{pmatrix} D_{xx} & 0 & 0 \\ 0 & D_{yy} & 0 \\ 0 & 0 & D_{zz} \end{pmatrix}$. Such DMI favors the formation of Bloch-type spin spirals [67–69].

Nanotube composed of entangling of more than single-helical nanoribbon is the extension of concept of helical nanoribbon. Similar to carbon nanotube [70], we can use two linearly independent vectors \mathbf{x} and \mathbf{y} to describe our system, as shown in Fig. 1(c). In this way we can set arbitrary chiral vectors in terms of integer indices pair (n, m) [71]: $\mathbf{R} = nx + my$, where m and n are integers. Then, we can divide nanotubes into three types: $n = m$ “armchair” nanotubes; $n = 0$ and $m \neq 0$ ($n \neq 0$ and $m = 0$) “zigzag” nanotubes; $n \neq m$ and $n, m \neq 0$ “chirality” nanotubes, respectively (see Fig. S5 within the Supplemental Material, SM [72]). While rolling up 2D magnet along y direction, achiral nanotubes can be formed. It is readily seen that corresponding nanotubes contain i . According to Moriya symmetry rules [2], DMI does not exist because of presence of i . Let us further investigate the chiral nanotubes wrapped along \mathbf{R} vector, which can be described through line group symmetry $\mathbf{L} = \mathbf{ZP}$ in mathematics (\mathbf{Z} indicates generalized translation group and \mathbf{P} is point factor) [73,74]. Importantly, such systems will break σ_v (vertical mirror), σ_h (horizontal mirror), i symmetries and an uncompensated DMI parameter will be induced. According to previous theoretical reports [73], the nanotubes rolled from 2D magnets, i.e., CrN, TMDs, CrI₃, VSe, and Cr₂Se₃, chosen in our calculations have following correspondence of the axial point group D_n . In this case, we can write the DMI tensor as $\begin{pmatrix} D_{xx} & 0 & 0 \\ 0 & D_{xx} & 0 \\ 0 & 0 & D_{zz} \end{pmatrix}$, which favors the Bloch-type chiral magnetisms. Under this condition, the w_{DM} can be further read as $w_{DM} = D_{xx}\mathcal{L}_{yz}^{(x)} + D_{yy}\mathcal{L}_{zx}^{(y)} + D_{zz}\mathcal{L}_{xy}^{(z)}$ based on $\mathcal{L}_{ij}^{(k)}$. Given that the D_n point group symmetry requires $D_{xx} = D_{yy}$, and $\mathcal{L}_{zx}^{(y)} = -\mathcal{L}_{xz}^{(y)}$, the above expression can be further simplified to $w_{DM} = D_{xx}(\mathcal{L}_{yz}^{(x)} - \mathcal{L}_{xz}^{(y)}) + D_{zz}\mathcal{L}_{xy}^{(z)}$.

A. Bloch-type DMI in chiral nanoribbon

To confirm our conceptual model, we first focus on the simpler 1D CrBr₂ nanoribbons [41]. As is shown in Fig. 2(a), CrBr₂ consists of edge-sharing CrBr₄ squares along the \mathbf{x} axis. Figure S2 within the SM [72] displays a schematic illustration of formation process of helical nanoribbon, which can be formed via rolling up a $16 \times 1 \times 1$ nanoribbon along the \mathbf{R} direction. We perform the noncollinear spin-polarized DFT to investigate chiral geometry-induced DMI properties. Figure 2(b) presents the homogeneous magnetizations rotating from $+z$ to $-z$ for a Néel-type spin spirals (upper parts) in the z - y plane and from $+x$ to $-x$ for a Bloch-type spin spirals (lower parts) in the x - y plane, respectively. Calculations of spin spiral energy $E(q)$ and DMI energy $\Delta E_{DMI}(q)$ are performed for chiral CrBr₂ nanoribbon [top part of Fig. 2(e)],

where the obtained results show only Bloch-type DMI will be induced in the presence of SOC [middle part of Fig. 2(e)]. We find that SOC arising from Br atoms of CrBr₂, which largely plays a dominant role in the existence of DMI [bottom part of Fig. 2(e)], will mediate the Bloch-type spin spirals for chiral nanoribbons. Instead, once SOC is neglected, as expected, $E(q)$ will become symmetric, where Bloch-type DMI disappears [red dotted square of Fig. 2(e)]. Above calculated results are consistent with mentioned analysis of quasi-one-dimensional model. Since both 2D materials and topological spin textures are current hot topics, there is no loss of generality that we further explore whether Bloch-type DMI also exist in chiral geometry-driven 2D magnets.

B. Bloch-type DMI in chiral nanotubes

Monolayer CrN recently has been predicted as a FM metal with high Curie temperature [72,75], its simpler structure is very beneficial for our comprehensive analysis of physical properties of magnetic nanotubes {see Figs. S1(a) and S1(b) within the SM [72]}. CrN with a small buckling can be viewed as consisting of two layers of N and Cr triangular lattices. When it is wrapped into chiral nanotubes, they can be regarded as double-walled nanotubes composed of triangular N and Cr nanotubes in Figs. S3(a) and S4(a) within the SM [72]. From our symmetry analysis, we can understand achiral nanotubes will not allow the presence of DMI, which can be further verified through DFT performed for achiral (2, 2) and (3, 0) CrN nanotubes [Fig. 3(c)]. When SOC is included, calculated spin spiral energy $E(q)$ and DMI energy $\Delta E_{DMI}(q)$ with $+q$ and $-q$ are degenerate, and the ground state is the FM state ($q = 0$). The results obtained indicate that DMI vanishes achiral configurations {Figs. S11(a) and S11(b) within the SM [72]}.

For chiral (1, 2) nanotube, we give the DFT results in Fig. 2(f). It can be seen that spin spiral energy $E(q)$ become asymmetric including SOC, where the spin spiral chirality favors to clockwise (CW) for (1, 2) because of the presence of DMI. Consistent with chiral CrBr₂ nanoribbon, chiral nanotube can give rise to Bloch-type DMI, while Néel-type DMI remains zero [middle part of Fig. 2(f)]. Once SOC is precluded, as expected, energy of spin spirals with q and $-q$ become degenerate [top part of Fig. 2(f)]. Concurrently, to understand the microscopic source of DMI, we plot the atomic-layer-resolved contribution of DMI energy $\Delta E_{DMI}(q)$ in bottom part of Fig. 2(f). One can see that $\Delta E_{DMI}(q)$ mainly stems from the magnetic Cr and nonmagnetic N has a negligible contribution, which is similar to previous report [34]. Next, we explore that effective DMI parameters as a function of diameter d of chiral nanotube, which can be defined as $d = \frac{a\sqrt{3(m^2+n^2+mn)}}{\pi}$ [76] and a represents the bond length of first-neighbor Cr and N atoms. Our calculations are performed for $(n, 2n)$ nanotubes, which correspond to d from 2.69 Å for (1, 2) to 10.74 Å for (5, 10) {Figs. 2(d), and also S9 and S10 within the SM [72]}. One can see that the DMI parameters exhibit an oscillatory dependence on the d , while the overall DMI strength shows a decreasing tendency with the increase of d , which can be ascribed to the weakening of curvature-induced inversion-symmetry breaking as the nanotube approaches the flat 2D limit.

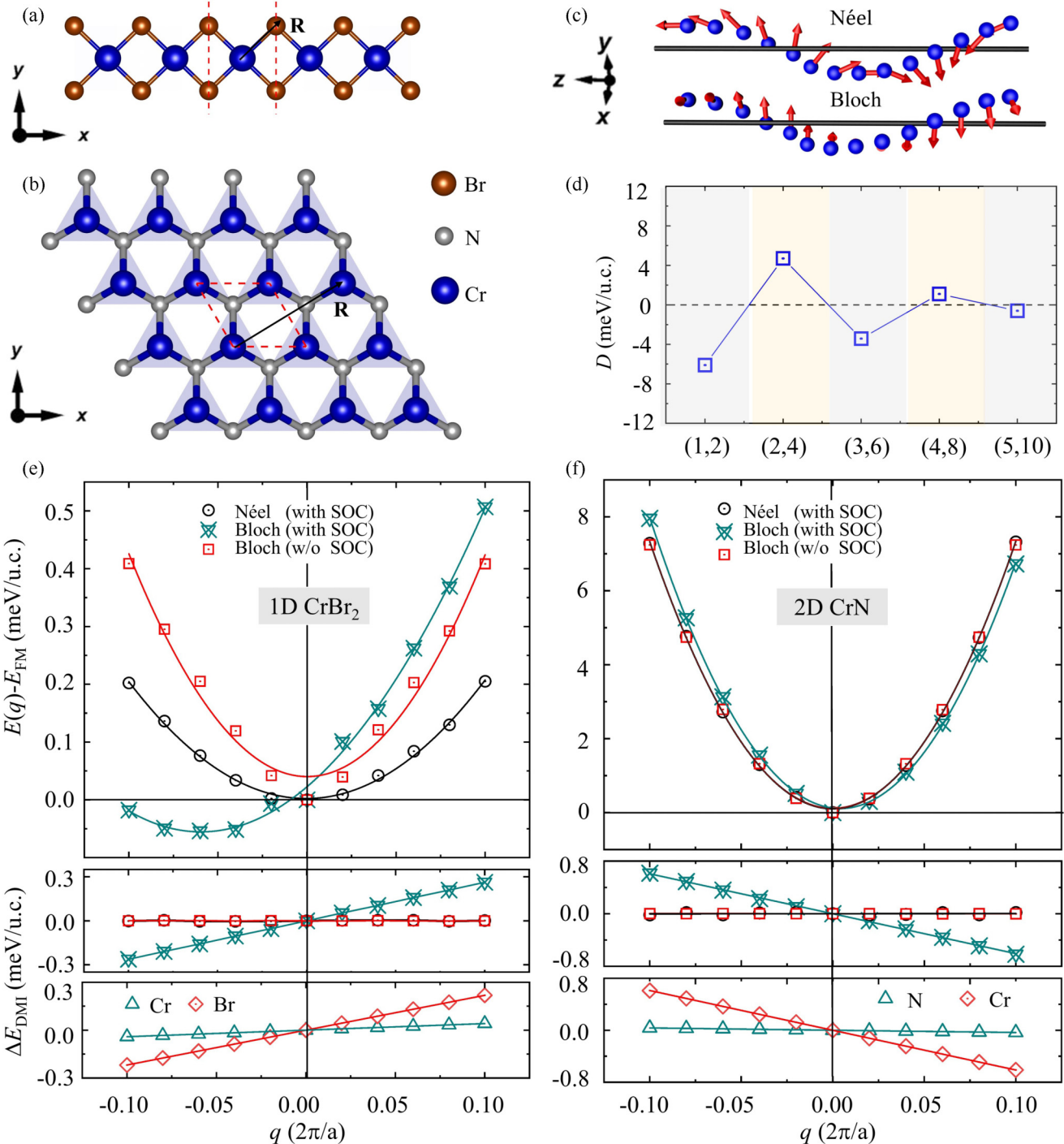


FIG. 2. Crystal structures of (a) quasi-one-dimensional CrBr₂ and (b) 2D CrN magnets, and rolling up the nanoribbon and nanotube along the \mathbf{R} direction. (c) Schematic magnetization rotating for a Néel-type (lower part) spin spirals in the z - y plane and for a Bloch-type (upper parts) spin spirals in the x - y plane used to calculate DMI. (d) Calculated DMI parameters as a function of CrN nanotube radius d ranging from 2.69 Å for (1, 2) to 10.74 Å for (5, 10). Calculated spin spiral energy $E(q)$ and DMI energy $\Delta E_{DMI}(q)$ as a function of spin spiral length q along the Γ - Z direction in (e) CrBr₂ chiral nanoribbon and (f) CrN chiral nanotube with (w/o) SOC, respectively. $E(q)$ at $q = 0$ represents the energy of FM state.

C. Chiral geometry-driven chiral DMI

Both geometric chirality and magnetic chirality can divide into two types of chirality: left- and right-handedness for the former [Fig. 3(a)], and CW and anticlockwise (ACW) chirality for the latter [Fig. 3(b)]. Geometry chirality will break i ,

resulting in spin chirality. It is interesting to ask if there a subtle connection between them, that is to say the chirality of materials corresponds to the chirality of the DMI. Accordingly, we introduce an interesting chiral parameter called helicity angle θ . The helicity angle θ of chiral nanotube can

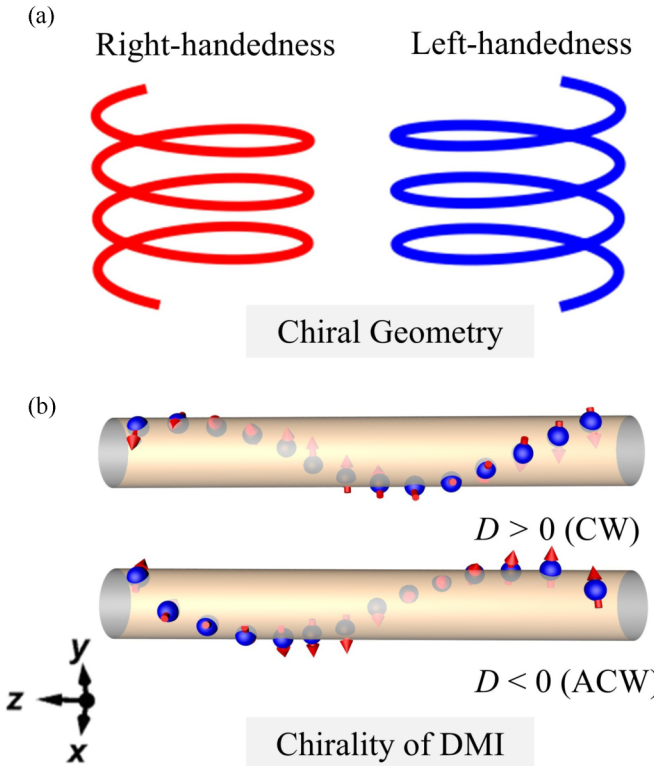
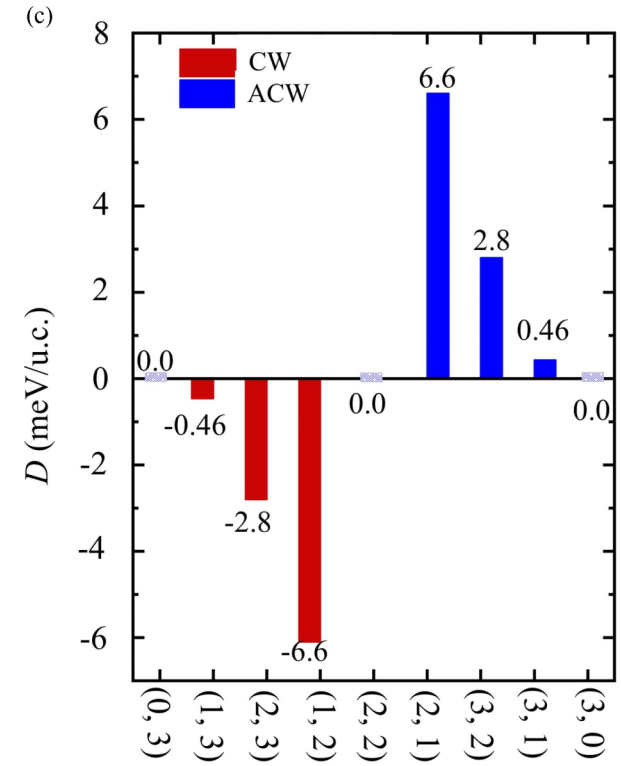


FIG. 3. (a) Schematic helical structures with different handedness. (b) Schematic spin configurations with opposite DMI chirality rotating in the z - y plane for Bloch-type spin spirals. (c) Calculated DMI parameters corresponding to CrN nanotubes with opposite handedness.

be defined via following formula [77]: $\cos \theta = \frac{2n+m}{2\sqrt{m^2+n^2+mn}}$, where $\theta = 0$ corresponds to “zigzag” configuration and $\theta = \frac{\pi}{6}$ is “armchair” one while $\theta \in (0, \frac{\pi}{6})$ represents chiral nanotube. We investigate the significant Bloch-type DMI between $\theta \in (0, \frac{\pi}{6})$ [Figs. 3(c)]. Interestingly, for chiral indices $(2, 1)$, $(3, 2)$, and $(3, 1)$, ACW spin spirals is favorable, while for nanotubes with opposite indices $(1, 2)$, $(2, 3)$, and $(1, 3)$, CW spin spirals become more favorable {Figs. S8, S11(c), and S11(d) within the SM [72]}. Our findings indicate that geometry engineering can serve as a paradigm for inducing Bloch-type DMI with opposite chirality, which can be useful to develop future logic devices.

To generalize our proposal for chiral geometry-driven Bloch-type DMI, we consider such effect in reported 2D magnets including TMDs, VSe, CrI₃, and Cr₂Se₃ (Figs. S2 and S3 within the SM [72]). All details for the calculations are presented in the SM [72]. Here, we concentrate on the calculated results of TMDs. For achiral TMDs nanotubes, symmetry analysis dictates that DMI of whole nanotubes will disappear, which is in line with calculated DMI parameters of the achiral magnetic nanotubes for chosen 2D materials {Figs. S12(a)–S12(f) within the SM [72]}. Meanwhile, Figs. S11(e) and S11(f) display asymmetric energy dispersions $E(q)$ including SOC of $(4, 2)$ CrSe₂ and $(6, 3)$ VSe chiral nanotubes. With the calculated $\Delta E_{\text{DMI}}(q)$ showing similar phenomenon to that of chiral CrN nanotubes, Bloch-type DMI is more favorable, while Néel-type DMI disappears. Once SOC effect is neglected in Fig. S7(b) within the SM [72], one can see that calculated DMI energy $\Delta E_{\text{DMI}}(q)$ becomes zero because of the symmetric energy dispersion for both $E(q)$ and $E(-q)$.



Finally, we summarize all calculated results for studied nanotubes in Table I, where only Bloch-type DMI can be induced in chiral nanotube. This is also consistent with our symmetric analysis under 2D model.

D. Proposal for chiral geometry-driven topological magnetism

Realizing topological magnetisms in reported nanotubes remains a missing piece. To explore the possibility of

TABLE I. Calculated Bloch-type DMI parameters D (meV/magnetic atom) of chiral, armchair, and zigzag nanotubes and first-neighbor exchange coupling J_1 (meV/magnetic atom) of chiral nanotubes.

Nanotube	Chirality			Armchair		Zigzag	
	(n, m)	D	J_1	(n, m)	D	(n, m)	D
CrN	$(2, 1)$	0.100	52.51	$(3, 3)$	0	$(3, 0)$	0
	$(3, 1)$	0.004	43.10				
	$(3, 2)$	0.016	33.35	$(5, 5)$	0	$(4, 0)$	0
	$(4, 2)$	-0.036	13.73				
	$(6, 3)$	0.014	31.69			$(5, 0)$	0
	$(8, 4)$	-0.004	40.94				
	$(10, 5)$	0.002	56.00				
CrSe ₂	$(4, 2)$	-0.041	13.61	$(6, 6)$	0	$(7, 0)$	0
MnSe ₂	$(4, 2)$	-0.013	-13.77	$(6, 6)$	0	$(7, 0)$	0
VSe ₂	$(6, 3)$	-0.090	12.26	$(4, 0)$	0	$(7, 0)$	0
VS ₂	$(6, 3)$	-0.040	3.14				
VSe	$(6, 3)$	-0.207	16.89	$(6, 6)$	0	$(7, 0)$	0
CrI ₃	$(5, 1)$	0.121	9.26	$(6, 6)$	0		
Cr ₂ Se ₃	$(5, 4)$	0.081	109.64	$(3, 3)$	0	$(7, 0)$	0

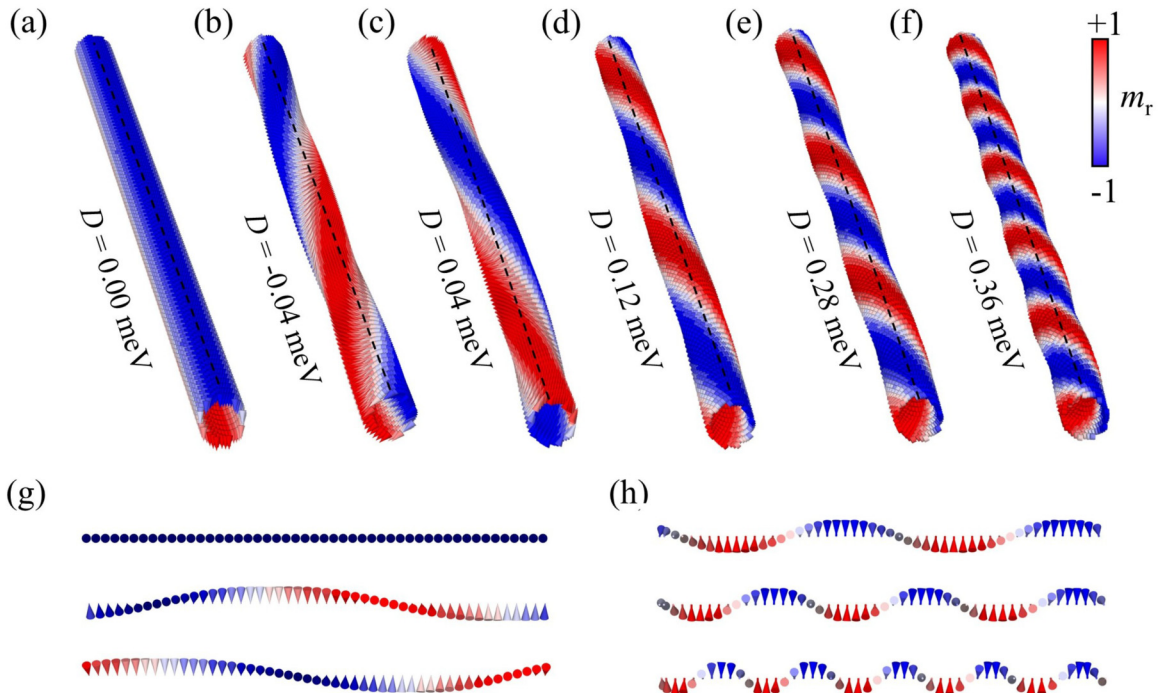


FIG. 4. Simulated chirality-dependent Bloch-type DW with (a) $D = 0$, (b) $D > 0$, and (c) $D < 0$ in VS_2 (6, 3) chiral nanotubes under periodic boundary conditions based on Monte Carlo method. Panels (d)–(f) illustrate the variation of spin spiral length of Bloch-type DW with increasing DMI. Panels (g) and (h) show Bloch-type spin spirals corresponding to the spins along the axial direction of the black dashed lines in (a)–(f).

noncollinear magnetism in chiral nanotubes, we calculate first-neighbor exchange coupling constant J_1 , DMI parameter D , and magnetic anisotropy K of chiral (6, 3) VS_2 nanotubes, respectively. Detailed methods are described in Appendix A. While all magnetic parameters are obtained, we perform Monte Carlo simulations to determine steady states of system under periodic (open) boundary conditions (Figs. 4 and also S14 within the SM [72]). Very interestingly, our simulations show that Bloch-type chiral DW with opposite chirality can be realized in chiral (6, 3) and (3, 6) VS_2 nanotubes [Figs. 4(a) and 4(c)]. This suggests that the chirality of DMI and noncollinear spin textures is closely coupled with the helical direction of chiral geometry. Noncollinear spin textures can also emerge from competing exchange interactions in frustrated magnets, independent of relativistic effects [78,79]. We further simulate the magnetic configurations under the scenario where the second-neighbor exchange interaction (J_2) is AFM coupling. As shown in Fig. S15 within the SM [72], DWs can still be induced in the absence of DMI. However, the chirality of these DWs varies randomly with increasing strength of the J_2 , in contrast to the deterministic chirality of DWs induced by the DMI. Otherwise, there is a continuous increase in DMI in chiral nanotubes with the increasing helicity angle θ , as shown in Fig. 3(c). Consequently, we are intrigued by the influence of DMI on Bloch-type DWs. It is evident that the spin spiral length of Bloch-type DWs shows a decreasing tendency with increasing DMI [Figs. 4(d)–4(f)]. Figures 4(g) and 4(h) show the Bloch-type spin spirals corresponding to spins of black dashed lines of Figs. 4(a)–4(f) along the axial direction. Once DMI is neglected, a uniform

FM state will emerge in Fig. 4(a). To understand the formation of a collinear spin structure in the absence of DMI, we simulate the atomic spin configurations under periodic boundary conditions for the chiral CrBr_2 nanoribbon [Figs. S16(a) and S16(b)] and the chiral VS_2 nanotube [Figs. S16(c) and S16(d)] within the SM [72]. When $J_1 > K$, the system exhibits a nearly collinear spin structure, whereas for $J_1 < K$, the spins tend to align in a tangential (helical) arrangement along the nanoribbon or nanotube. The inclusion of DMI then induces a well-defined chiral modulation of this collinear state, giving rise to the observed spiral textures. In addition, under periodic boundary conditions, we perform Landau-Lifshitz-Gilbert (LLG) dynamics simulations starting from random initial states to validate the reliability of our simulation results (see Appendix B), as shown in Fig. 5. We also find that the DMI plays a crucial role in both the formation and chirality of the DWs. The above phenomenon strongly suggests that the formation of Bloch-type DW originates from DMI induced by SOC. We believe that chirality engineering can serve as a paradigm for realizing a rich variety of topological magnetic textures, such as skyrmions and bimerons, based on pure 2D magnets.

III. CONCLUSIONS

In conclusion, chirality-dependent DMI, arising from intrinsic geometric features, offer a general strategy to engineer diverse spin states in low-dimensional magnets. We propose chiral geometries with D_n crystal symmetry as a route to crystal-symmetry-protected Bloch-type DMI. The missing elements for realizing topological magnetism in

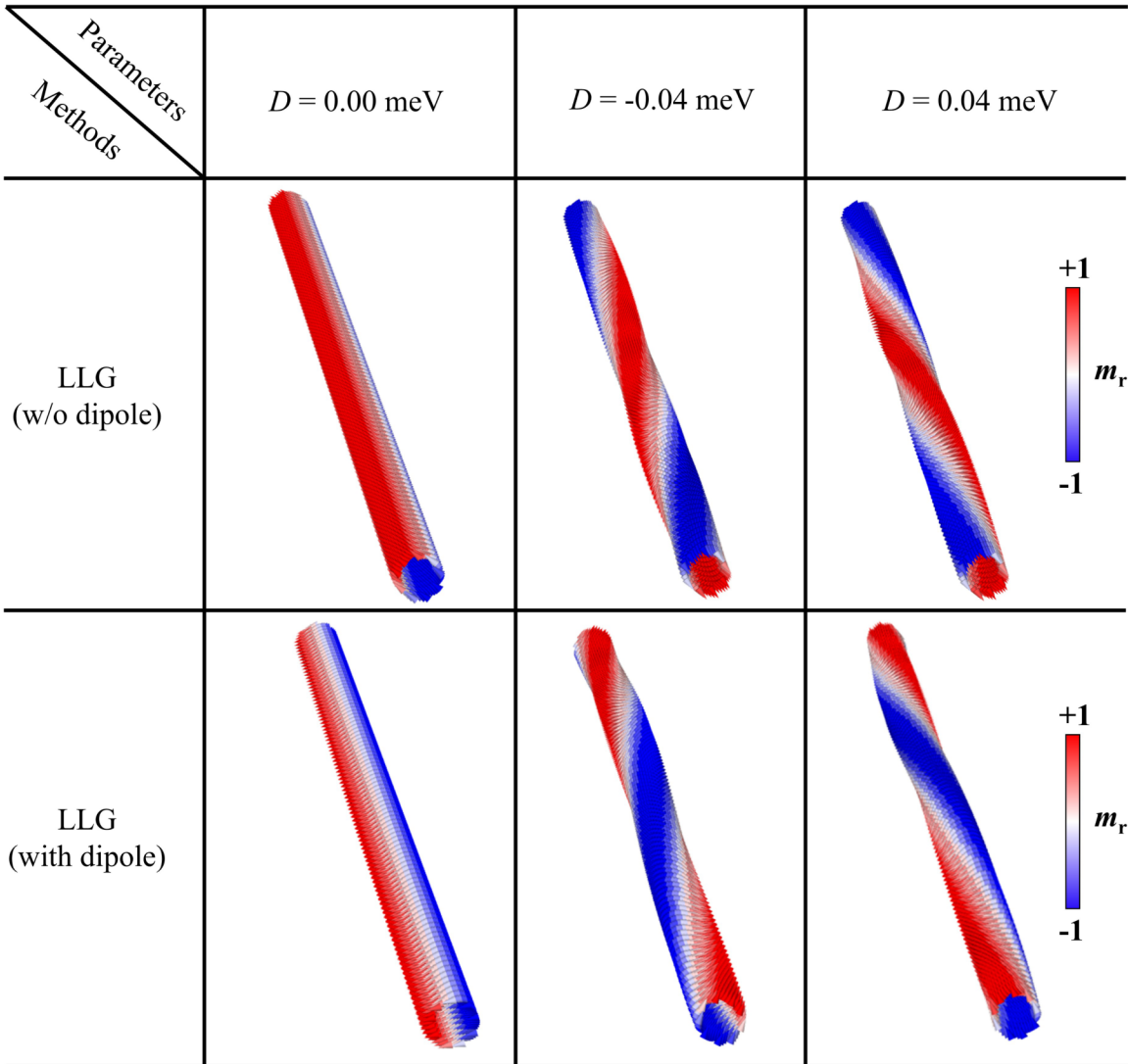


FIG. 5. Simulated chirality-dependent Bloch-type DW with $D = 0$, $D > 0$ and $D < 0$ in VS_2 (6, 3) chiral nanotubes with (w/o) dipole-dipole interactions under periodic boundary conditions based on LLG equation.

quasi-one-dimensional systems are identified. Symmetry analysis and numerical simulations confirm the emergence of Bloch-type DMI and DWs in these chiral geometry-driven magnets derived from diverse 2D magnetic systems. Remarkably, the intrinsic coupling between geometric and magnetic chirality is revealed, where the chirality of DMI and non-collinear states is locked to the handedness of the underlying geometry. The results obtained here, open this unexplored domain, expanding the research landscape of topological magnetism, pave the way for the development of future chiral geometry-based spintronic devices.

ACKNOWLEDGMENTS

This work was supported by the National Natural Science Foundation of China (Grants No. 12204497, No. 12174405, No. T2495212, and No. 12474114), the National Key Research and Development Program of China (Grant No. 2022YFA1405100), Ningbo Key Scientific and Technological Project (Grant No. 2021000215), China Postdoctoral Science

Foundation (Grant No. 2025M773336), and the Postdoctoral Fellowship Program of CPSF (Grant No. GZC20252195).

DATA AVAILABILITY

The data that support the findings of this article are not publicly available. The data are available from the authors upon reasonable request.

APPENDIX A: COMPUTATIONAL DETAILS OF MAGNETIC PARAMETERS

Dzyaloshinskii-Moriya interaction (DMI) D. We have implemented the qSO methods based on the generalized Bloch theorem to calculate spin spiral energy $E(q)$ in the interval of q from $-0.1(\frac{2\pi}{a})$ to $+0.1(\frac{2\pi}{a})$ by a self-consistent way along the Γ -Z direction, where SOC is treated within first-order perturbation theory [65,66,80]. In our calculations, we consider that noncollinear spin spirals structures rotate along the axis direction of nanotube parallel to z axis. Such spirals corresponding to Bloch- and Néel-type have

following expression: $\mathbf{m} = [\sin(\mathbf{q} \cdot \mathbf{r}_i), \cos(\mathbf{q} \cdot \mathbf{r}_i), 0]$ and $\mathbf{m} = [0, \sin(\mathbf{q} \cdot \mathbf{r}_i), \cos(\mathbf{q} \cdot \mathbf{r}_i)]$ for spin moments at site \mathbf{r}_i and \mathbf{q} represents spin spiral vector, respectively. For small $\mathbf{q} = (q, 0, 0)$ vector, we can obtain the DMI energy $\Delta E_{\text{DMI}}(q)$ via solving the energy difference of two spirals with opposite chirality: $\Delta E_{\text{DMI}}(q) = [E(q) - E(-q)]/2$. Then, we can estimate the DMI values as $\Delta E_{\text{DMI}}(q) \propto Dq$. Here, positive D favors spin configuration of ACW chirality, and a negative one represents CW chirality. Besides, we use $1 \times 1 \times 4, 1 \times 1 \times 6, 1 \times 1 \times 4, 1 \times 1 \times 4, 1 \times 1 \times 4 (2 \times 2 \times 8, 2 \times 2 \times 8, 1 \times 1 \times 4, 2 \times 2 \times 8)$ k-mesh points for chiral CrBr_2 , CrN , TMDs, VSe, CrI_3 , and Cr_2Se_3 (achiral CrN , TMDs, VSe, CrI_3 , and Cr_2Se_3) nanotubes in spin-spiral energy calculations. Clearly, we also test $1 \times 1 \times 8$ k-mesh points for chiral vector $(2, 1) \text{ CrN}, (4, 2) \text{ CrSe}_2$ nanotubes, calculated results do not change a lot [see Figs. S7(c) and S7(d) within the SM [72]].

Magnetic anisotropy K. In calculations, we show three magnetic states, in which all spins are magnetized along the axial, tangential, and radial directions of nanotubes with corresponding energy E_ζ , E_φ , and E_r . For flat 2D magnets, magnetic anisotropy energy can be identified as energy difference between in-plane (100) and out-of-plane (001) magnetized axis. Here, we can obtain the effective magnetic anisotropy K via solving

$$K = E_{\varphi(\zeta)} - E_r, \quad (\text{A1})$$

Heisenberg exchange coupling J. The energy mapping methods are performed to calculate the Heisenberg exchange coupling constant J . First, structural relaxation is performed until the forces acting on each atom are smaller than 0.001 eV/Å for determining the ground state of nanotube geometry. Next, we construct the FM and antiferromagnetic (AFM) configuration to determine the self-consistent total energy of supercell in the absence of SOC, as is depicted in Fig. S13 within the SM [72]. In this way, we can solve first-neighbor exchange coupling constant J_1 of VS_2 (6, 3) chiral nanotubes via following equations:

$$E_{\text{FM}} = -\frac{1}{2} \times 42 \times (6J_1) + E_0, \quad (\text{A2})$$

$$E_{\text{AFM}} = -\frac{1}{2} \times 42 \times (-2J_1) + E_0, \quad (\text{A3})$$

$$J_1 = \frac{E_{\text{AFM}} - E_{\text{FM}}}{168}, \quad (\text{A4})$$

where E_0 represents the total energy of system without (w/o) the Heisenberg exchange coupling interaction and positive/negative J_1 indicate FM/AFM coupling.

APPENDIX B: ATOMIC SPIN MODEL SIMULATIONS

We perform the atomistic spin model simulation based on obtained magnetic parameters from DFT within the VAMPIRE package [81] for magnetization dynamics simulations of chiral magnetic nanotube. Then, the LLG equations is given to describe the dynamics of atomic spins,

$$\frac{\partial \mathbf{S}_i}{\partial t} = -\frac{\gamma}{(1+\lambda^2)} [\mathbf{S}_i \times \mathbf{B}_{\text{eff}}^i + \lambda \mathbf{S}_i \times (\mathbf{S}_i \times \mathbf{B}_{\text{eff}}^i)]. \quad (\text{B1})$$

Here, γ is the gyromagnetic ratio, λ is the gilbert damping constant, and \mathbf{S}_i is the unit vector, which is defined as $\frac{\mu_i}{|\mu_i|}$, where μ_i represents the magnetic moment of i th magnetic atom. Meantime, the absolute value of the gyromagnetic ratio is determined as $\gamma = 1.76 \times 10^{11} \text{ T}^{-1} \text{ s}^{-1}$ and damping constant λ is choose as 0.2. $\mathbf{B}_{\text{eff}}^i$ is the effective magnetic field on each \mathbf{S}_i and can be obtained by following equation: $\mathbf{B}_{\text{eff}}^i = -\frac{1}{\mu_s} \frac{\partial H}{\partial \mathbf{S}_i}$, in which H represents the total spin Hamiltonian. Subsequently, the system's spin Hamiltonian can be written as

$$H = - \sum_{\langle i, j \rangle} \mathbf{D}_{ij} \cdot (\mathbf{S}_i \times \mathbf{S}_j) - J_1 \sum_{\langle i, j \rangle} (\mathbf{S}_i \cdot \mathbf{S}_j) - K \sum_{\langle i \rangle} (\mathbf{S}_i^\varphi)^2, \quad (\text{B2})$$

where $\langle i, j \rangle$ are the summation of magnetic atoms pairs and \mathbf{S}_i and \mathbf{S}_j represent the normal spin vector at the site i and j . \mathbf{S}_i^φ indicate spins are magnetized along the easy-axis direction. \mathbf{D}_{ij} , J_1 , and K are referred as DMI vector, Heisenberg exchange coupling, and magnetic anisotropy. DMI parameters D is obtained from Table I. Based on above computational methods of magnetic parameters, computed J_1 , K of chiral (6, 3) VS_2 nanotube are 3.14 meV/V atom, 0.08 meV/V atom. Monte Carlo simulations with Metropolis algorithm are applied with above spin Hamiltonian of Eq. (B2) to explore final magnetic states of chiral nanotubes. In all simulations, we choose a $0.95 \times 0.95 \times 140 \text{ nm}^3$ nanotube with periodic boundary condition along the z direction.

-
- [1] I. Dzyaloshinsky, A thermodynamic theory of “Weak” ferromagnetism of antiferromagnetics, *J. Phys. Chem. Solids* **4**, 241 (1958).
 - [2] T. Moriya, Anisotropic superexchange interaction and weak ferromagnetism, *Phys. Rev.* **120**, 91 (1960).
 - [3] A. Thiaville, S. Rohart, É. Jué, V. Cros, and A. Fert, Dynamics of Dzyaloshinskii domain walls in ultrathin magnetic films, *Europhys. Lett.* **100**, 57002 (2012).
 - [4] K. S. Ryu, L. Thomas, S. H. Yang, and S. Parkin, Chiral spin torque at magnetic domain walls, *Nat. Nanotechnol.* **8**, 527 (2013).
 - [5] M. Bode, M. Heide, K. von Bergmann, P. Ferriani, S. Heinze, G. Bihlmayer, A. Kubetzka, O. Pietzsch, S. Blugel, and R. Wiesendanger, Chiral magnetic order at surfaces driven by inversion asymmetry, *Nature (London)* **447**, 190 (2007).
 - [6] A. N. Bogdanov and D. Yablonskii, Thermodynamically stable “vortices” in magnetically ordered crystals. The mixed state of magnets, *Sov. Phys. JETP* **68**, 101 (1989).
 - [7] S. Mühlbauer, B. Binz, F. Jonietz, C. Pfleiderer, A. Rosch, A. Neubauer, R. Georgii, and P. Böni, Skyrmiion lattice in a chiral magnet, *Science* **323**, 915 (2009).
 - [8] X. Z. Yu, Y. Onose, N. Kanazawa, J. H. Park, J. H. Han, Y. Matsui, N. Nagaosa, and Y. Tokura, Real-space observation of a two-dimensional skyrmion crystal, *Nature (London)* **465**, 901 (2010).

- [9] B. Göbel, A. Mook, J. Henk, I. Mertig, and O. A. Tretiakov, Magnetic bimerons as skyrmion analogues in in-plane magnets, *Phys. Rev. B* **99**, 060407(R) (2019).
- [10] H. Jani, J. C. Lin, J. Chen, J. Harrison, F. Maccherozzi, J. Schad, S. Prakash, C. B. Eom, A. Ariando, T. Venkatesan, and P. G. Radaelli, Antiferromagnetic half-skyrmions and bimerons at room temperature, *Nature (London)* **590**, 74 (2021).
- [11] I. Dzyaloshinskii, Theory of helicoidal structures in antiferromagnets, I. Nonmetals, Sov. Phys. JETP **19**, 960 (1964).
- [12] L. D. Landau and E. M. Lifshitz, *Course of Theoretical Physics* (Elsevier, New York, 2013).
- [13] Y. Tokura and N. Kanazawa, Magnetic skyrmion materials, *Chem. Rev.* **121**, 2857 (2020).
- [14] A. Fert, N. Reyren, and V. Cros, Magnetic skyrmions: Advances in physics and potential applications, *Nat. Rev. Mater.* **2**, 17031 (2017).
- [15] H. Yang, A. Thiaville, S. Rohart, A. Fert, and M. Chshiev, Anatomy of Dzyaloshinskii-Moriya Interaction at Co/Pt interfaces, *Phys. Rev. Lett.* **115**, 267210 (2015).
- [16] M. Schott, A. Bernand-Mantel, L. Ranno, S. Pizzini, J. Vogel, H. Bea, C. Baraduc, S. Auffret, G. Gaudin, and D. Givord, The skyrmion switch: Turning magnetic skyrmion bubbles on and off with an electric field, *Nano Lett.* **17**, 3006 (2017).
- [17] H. Yang, G. Chen, A. A. C. Cotta, A. T. N'Diaye, S. A. Nikolaev, E. A. Soares, W. A. A. Macedo, K. Liu, A. K. Schmid, A. Fert, and M. Chshiev, Significant Dzyaloshinskii-Moriya interaction at graphene-ferromagnet interfaces due to the Rashba effect, *Nat. Mater.* **17**, 605 (2018).
- [18] O. Boulle, J. Vogel, H. Yang, S. Pizzini, D. de Souza Chaves, A. Locatelli, T. O. Mentes, A. Sala, L. D. Buda-Prejbeanu, O. Klein, *et al.*, Room-temperature chiral magnetic skyrmions in ultrathin magnetic nanostructures, *Nat. Nanotechnol.* **11**, 449 (2016).
- [19] G. Chen, M. Robertson, M. Hoffmann, C. Ophus, A. L. Fernandes Cauduro, R. Lo Conte, H. Ding, R. Wiesendanger, S. Blügel, A. K. Schmid, and K. Liu, Observation of hydrogen-induced Dzyaloshinskii-Moriya interaction and reversible switching of magnetic chirality, *Phys. Rev. X* **11**, 021015 (2021).
- [20] G. Chen, A. Mascaraque, H. Jia, B. Zimmermann, M. Robertson, R. L. Conte, M. Hoffmann, M. A. González Barrio, H. Ding, R. Wiesendanger, *et al.*, Large Dzyaloshinskii-Moriya interaction induced by chemisorbed oxygen on a ferromagnet surface, *Sci. Adv.* **6**, eaba4924 (2020).
- [21] M. Kuepferling, A. Casiraghi, G. Soares, G. Durin, F. Garcia-Sánchez, L. Chen, C. H. Back, C. H. Marrows, S. Tacchi, and G. Carlotti, Measuring interfacial Dzyaloshinskii-Moriya interaction in ultrathin magnetic films, *Rev. Mod. Phys.* **95**, 015003 (2023).
- [22] D. Cortes-Ortuno and P. Landeros, Influence of the Dzyaloshinskii-Moriya interaction on the spin-wave spectra of thin films, *J. Phys. Condens. Matter* **25**, 156001 (2013).
- [23] A. K. Nayak, V. Kumar, T. Ma, P. Werner, E. Pippel, R. Sahoo, F. Damay, U. K. Rossler, C. Felser, and S. S. P. Parkin, Magnetic antiskyrmions above room temperature in tetragonal Heusler materials, *Nature (London)* **548**, 561 (2017).
- [24] Z. He, Z. Li, Z. Chen, Z. Wang, J. Shen, S. Wang, C. Song, T. Zhao, J. Cai, S. Z. Lin, Y. Zhang, and B. Shen, Experimental observation of current-driven antiskyrmion sliding in stripe domains, *Nat. Mater.* **23**, 1048 (2024).
- [25] K. Karube, L. Peng, J. Masell, X. Yu, F. Kagawa, Y. Tokura, and Y. Taguchi, Room-temperature antiskyrmions and sawtooth surface textures in a non-centrosymmetric magnet with S(4) symmetry, *Nat. Mater.* **20**, 335 (2021).
- [26] M. Hoffmann, B. Zimmermann, G. P. Muller, D. Schurhoff, N. S. Kiselev, C. Melcher, and S. Blugel, Antiskyrmions stabilized at interfaces by anisotropic Dzyaloshinskii-Moriya interactions, *Nat. Commun.* **8**, 308 (2017).
- [27] C. Gong and X. Zhang, Two-dimensional magnetic crystals and emergent heterostructure devices, *Science* **363**, eaav4450 (2019).
- [28] H. Yang, S. O. Valenzuela, M. Chshiev, S. Couet, B. Dieny, B. Dublak, A. Fert, K. Garello, M. Jamet, D. E. Jeong, *et al.*, Two-dimensional materials prospects for non-volatile spintronic memories, *Nature (London)* **606**, 663 (2022).
- [29] M. Gibertini, M. Koperski, A. F. Morpurgo, and K. S. Novoselov, Magnetic 2D materials and heterostructures, *Nat. Nanotechnol.* **14**, 408 (2019).
- [30] J. Liang, W. Wang, H. Du, A. Hallal, K. Garcia, M. Chshiev, A. Fert, and H. Yang, Very large Dzyaloshinskii-Moriya interaction in two-dimensional Janus manganese dichalcogenides and its application to realize skyrmion states, *Phys. Rev. B* **101**, 184401 (2020).
- [31] C. Xu, J. Feng, S. Prokhorenko, Y. Nahas, H. Xiang, and L. Bellaiche, Topological spin texture in janus monolayers of the chromium trihalides Cr(I,X)3, *Phys. Rev. B* **101**, 060404(R) (2020).
- [32] Z. Shao, J. Liang, Q. Cui, M. Chshiev, A. Fert, T. Zhou, and H. Yang, Multiferroic materials based on transition-metal dichalcogenides: Potential platform for reversible control of Dzyaloshinskii-Moriya interaction and skyrmion via electric field, *Phys. Rev. B* **105**, 174404 (2022).
- [33] G. Zheng, M. Wang, X. Zhu, C. Tan, J. Wang, S. Albarakati, N. Aloufi, M. Algarni, L. Farrar, M. Wu, *et al.*, Tailoring Dzyaloshinskii-Moriya interaction in a transition metal dichalcogenide by dual-intercalation, *Nat. Commun.* **12**, 3639 (2021).
- [34] J. Liang, Q. Cui, and H. Yang, Electrically switchable Rashba-type Dzyaloshinskii-Moriya interaction and skyrmion in two-dimensional magnetoelectric multiferroics, *Phys. Rev. B* **102**, 220409(R) (2020).
- [35] C. Xu, P. Chen, H. Tan, Y. Yang, H. Xiang, and L. Bellaiche, Electric-field switching of magnetic topological charge in type-I multiferroics, *Phys. Rev. Lett.* **125**, 037203 (2020).
- [36] W. Sun, W. Wang, H. Li, G. Zhang, D. Chen, J. Wang, and Z. Cheng, Controlling bimerons as skyrmion analogues by ferroelectric polarization in 2D van der Waals multiferroic heterostructures, *Nat. Commun.* **11**, 5930 (2020).
- [37] Y. Wu, S. Zhang, J. Zhang, W. Wang, Y. L. Zhu, J. Hu, G. Yin, K. Wong, C. Fang, C. Wan, *et al.*, Neel-type skyrmion in WTe₂/Fe₃GeTe₂ van der Waals heterostructure, *Nat. Commun.* **11**, 3860 (2020).
- [38] M. Akram, H. LaBollita, D. Dey, J. Kapeghian, O. Erten, and A. S. Botana, Moire skyrmions and chiral magnetic phases in twisted CrX₃ (X = I, Br, and Cl) bilayers, *Nano Lett.* **21**, 6633 (2021).
- [39] M. Akram and O. Erten, Skyrmions in twisted van der Waals magnets, *Phys. Rev. B* **103**, L140406 (2021).

- [40] B. Yang, Y. Li, H. Xiang, H. Lin, and B. Huang, Moiré magnetic exchange interactions in twisted magnets, *Nat. Comput. Sci.* **3**, 314 (2023).
- [41] Y. Ga, Q. Cui, J. Liang, D. Yu, Y. Zhu, L. Wang, and H. Yang, Dzyaloshinskii-Moriya interaction and magnetic skyrmions induced by curvature, *Phys. Rev. B* **106**, 054426 (2022).
- [42] Y. J. Zhang, T. Ideue, M. Onga, F. Qin, R. Suzuki, A. Zak, R. Tenne, J. H. Smet, and Y. Iwasa, Enhanced intrinsic photovoltaic effect in tungsten disulfide nanotubes, *Nature (London)* **570**, 349 (2019).
- [43] G. Seifert, H. Terrones, M. Terrones, G. Jungnickel, and T. Frauenheim, Structure and electronic properties of MoS₂ nanotubes, *Phys. Rev. Lett.* **85**, 146 (2000).
- [44] F. Qin, W. Shi, T. Ideue, M. Yoshida, A. Zak, R. Tenne, T. Kikitsu, D. Inoue, D. Hashizume, and Y. Iwasa, Superconductivity in a chiral nanotube, *Nat. Commun.* **8**, 14465 (2017).
- [45] B. Kim, N. Park, and J. Kim, Giant bulk photovoltaic effect driven by the wall-to-wall charge shift in WS₂ nanotubes, *Nat. Commun.* **13**, 3237 (2022).
- [46] W. Su, X. Li, L. Li, D. Yang, F. Wang, X. Wei, W. Zhou, H. Kataura, S. Xie, and H. Liu, Chirality-dependent electrical transport properties of carbon nanotubes obtained by experimental measurement, *Nat. Commun.* **14**, 1672 (2023).
- [47] F. Qin, T. Ideue, W. Shi, X. X. Zhang, M. Yoshida, A. Zak, R. Tenne, T. Kikitsu, D. Inoue, D. Hashizume, and Y. Iwasa, Diameter-dependent superconductivity in individual WS₂ nanotubes, *Nano Lett.* **18**, 6789 (2018).
- [48] D. D. Sheka, O. V. Pylypovskiy, P. Landeros, Y. Gaididei, A. Kákay, and D. Makarov, Nonlocal chiral symmetry breaking in curvilinear magnetic shells, *Commun. Phys.* **3**, 128 (2020).
- [49] F. Yang, X. Wang, D. Zhang, J. Yang, D. Luo, Z. Xu, J. Wei, J. Q. Wang, Z. Xu, F. Peng, *et al.*, Chirality-specific growth of single-walled carbon nanotubes on solid alloy catalysts, *Nature (London)* **510**, 522 (2014).
- [50] N. G. Chopra, R. J. Luyken, K. Cherrey, V. H. Crespi, M. L. Cohen, S. G. Louie, and A. Zettl, Boron nitride nanotubes, *Science* **269**, 966 (1995).
- [51] B. Liu, F. Wu, H. Gui, M. Zheng, and C. Zhou, Chirality-controlled synthesis and applications of single-wall carbon nanotubes, *ACS Nano* **11**, 31 (2017).
- [52] J. Liu, C. Wang, X. Tu, B. Liu, L. Chen, M. Zheng, and C. Zhou, Chirality-controlled synthesis of single-wall carbon nanotubes using vapour-phase epitaxy, *Nat. Commun.* **3**, 1199 (2012).
- [53] S. Aftab, M. Z. Iqbal, and Y. S. Rim, Recent advances in rolling 2d Tmds nanosheets into 1d Tmds nanotubes/nanoscrolls, *Small* **19**, e2205418 (2023).
- [54] D. Yang, L. Li, X. Li, W. Xi, Y. Zhang, Y. Liu, X. Wei, W. Zhou, F. Wei, S. Xie, and H. Liu, Preparing high-concentration individualized carbon nanotubes for industrial separation of multiple single-chirality species, *Nat. Commun.* **14**, 2491 (2023).
- [55] E. Josten, D. Raftrey, A. Hierro-Rodriguez, A. Sorrentino, L. Aballe, M. Lipińska-Chwałek, T. Jansen, K. Höflich, H. Kröncke, C. Dubourdieu, *et al.*, Curvature-mediated spin textures in magnetic multi-layered nanotubes, *arXiv:2103.13310*.
- [56] H. E. Lim, Y. Miyata, R. Kataura, Y. Nishimura, Y. Nishimoto, S. Irle, J. H. Warner, H. Kataura, and H. Shinohara, Growth of carbon nanotubes via twisted graphene nanoribbons, *Nat. Commun.* **4**, 2548 (2013).
- [57] G. Povie, Y. Segawa, T. Nishihara, Y. Miyauchi, and K. Itami, Synthesis of a carbon nanobelt, *Science* **356**, 172 (2017).
- [58] M. N. Gjerding, A. Taghizadeh, A. Rasmussen, S. Ali, F. Bertoldo, T. Deilmann, N. R. Knøsgaard, M. Kruse, A. H. Larsen, S. Manti, *et al.*, Recent progress of the computational 2D materials database (C2DB), *2D Mater.* **8**, 044002 (2021).
- [59] D. Torelli, H. Moustafa, K. W. Jacobsen, and T. Olsen, High-throughput computational screening for two-dimensional magnetic materials based on experimental databases of three-dimensional compounds, *npj Comput. Mater.* **6**, 158 (2020).
- [60] B. Li, Z. Wan, C. Wang, P. Chen, B. Huang, X. Cheng, Q. Qian, J. Li, Z. Zhang, G. Sun, B. Zhao, *et al.*, van der Waals epitaxial growth of air-stable CrSe₂ nanosheets with thickness-tunable magnetic order, *Nat. Mater.* **20**, 818 (2021).
- [61] D. J. O'Hara, T. Zhu, A. H. Trout, A. S. Ahmed, Y. K. Luo, C. H. Lee, M. R. Brenner, S. Rajan, J. A. Gupta, D. W. McComb, and R. K. Kawakami, Room temperature intrinsic ferromagnetism in epitaxial manganese selenide films in the monolayer limit, *Nano Lett.* **18**, 3125 (2018).
- [62] M. Bonilla, S. Kolekar, Y. Ma, H. C. Diaz, V. Kalappattil, R. Das, T. Eggers, H. R. Gutierrez, M. H. Phan, and M. Batzill, Strong room-temperature ferromagnetism in VSe₂ monolayers on van der Waals substrates, *Nat. Nanotechnol.* **13**, 289 (2018).
- [63] B. Huang, G. Clark, E. Navarro-Moratalla, D. R. Klein, R. Cheng, K. L. Seyler, D. Zhong, E. Schmidgall, M. A. McGuire, D. H. Cobden, *et al.*, Layer-dependent ferromagnetism in a van der Waals crystal down to the monolayer limit, *Nature (London)* **546**, 270 (2017).
- [64] J. Y. Chen, X. X. Li, W. Z. Zhou, J. L. Yang, F. P. Ouyang, and X. Xiong, Large-spin-gap nodal-line half-metal and high-temperature ferromagnetic semiconductor in Cr₂X₃ (X = O,S,Se) monolayers, *Adv. Electron. Mater.* **6**, 1900490 (2019).
- [65] L. M. Sandratskii, Insight into the Dzyaloshinskii-Moriya interaction through first-principles study of chiral magnetic structures, *Phys. Rev. B* **96**, 024450 (2017).
- [66] H. Yang, J. Liang, and Q. Cui, First-principles calculations for Dzyaloshinskii-Moriya interaction, *Nat. Rev. Phys.* **5**, 43 (2022).
- [67] A. Di Pietro, P. Ansalone, V. Basso, A. Magni, and G. Durin, Gauge theory applied to magnetic lattices, *Europhys. Lett.* **140**, 46003 (2022).
- [68] R. R. Birss, *Symmetry and Magnetism, Selected Topics in Solid State Physics* (North-Holland Publishing Co., Amsterdam, 1964).
- [69] H. Niu, H. Y. Kwon, T. Ma, Z. Cheng, C. Ophus, B. Miao, L. Sun, Y. Wu, K. Liu, S. S. P. Parkin, *et al.*, Reducing crystal symmetry to generate out-of-plane Dzyaloshinskii-Moriya interaction, *Nat. Commun.* **15**, 10199 (2024).
- [70] S. Iijima, Helical microtubules of graphitic carbon, *Nature (London)* **354**, 56 (1991).
- [71] N. Hamada, S. Sawada, and A. Oshiyama, New one-dimensional conductors: Graphitic microtubules, *Phys. Rev. Lett.* **68**, 1579 (1992).
- [72] See Supplemental Material at <http://link.aps.org/supplemental/10.1103/81rn-9t23> for (i) computational details for first-principles calculations, and (ii) structure analysis, which includes Refs. [64,82–92].

- [73] V. Kopsky and D. Litvin, *International Tables for Crystallography*, Vol. E, Subperiodic Groups (Kluwer Academic Publishers, London, 2002).
- [74] M. Damnjanović, B. Nikolić, and I. Milošević, Symmetry of nanotubes rolled up from arbitrary two-dimensional lattices along an arbitrary chiral vector, *Phys. Rev. B* **75**, 033403 (2007).
- [75] W. Luo, K. Xu, and H. Xiang, Two-dimensional hyperferroelectric metals: A different route to ferromagnetic-ferroelectric multiferroics, *Phys. Rev. B* **96**, 235415 (2017).
- [76] T. Yamabe, Recent development of carbon nanotube, *Synth. Met.* **70**, 1511 (1995).
- [77] M. Meo and M. Rossi, Prediction of young's modulus of single wall carbon nanotubes by molecular-mechanics based finite element modelling, *Compos. Sci. Technol.* **66**, 1597 (2006).
- [78] A. A. Gippius, E. N. Morozova, A. S. Moskvin, A. V. Zalessky, A. A. Bush, M. Baenitz, H. Rosner, and S. L. Drechsler, NMR and local-density-approximation evidence for spiral magnetic order in the chain cuprate LiCu_2O_2 , *Phys. Rev. B* **70**, 020406 (2004).
- [79] T. Masuda, A. Zheludev, A. Bush, M. Markina, and A. Vasiliev, Competition between helimagnetism and commensurate quantum spin correlations in LiCu_2O_2 , *Phys. Rev. Lett.* **92**, 177201 (2004).
- [80] M. Heide, G. Bihlmayer, and S. Blügel, Describing Dzyaloshinskii–Moriya spirals from first principles, *Phys. B* **404**, 2678 (2009).
- [81] B. Skubic, J. Hellsvik, L. Nordström, and O. Eriksson, A method for atomistic spin dynamics simulations: Implementation and examples, *J. Phys.: Condens. Matter* **20**, 315203 (2008).
- [82] G. Kresse and J. Furthmüller, Efficient iterative schemes for *ab initio* total-energy calculations using a plane-wave basis set, *Phys. Rev. B* **54**, 11169 (1996).
- [83] J. P. Perdew, K. Burke, and M. Ernzerhof, Generalized gradient approximation made simple, *Phys. Rev. Lett.* **77**, 3865 (1996).
- [84] G. Kresse and J. Hafner, *Ab initio* molecular dynamics for liquid metals, *Phys. Rev. B* **47**, 558 (1993).
- [85] G. Kresse and J. Furthmüller, Efficiency of ab-initio total energy calculations for metals and semiconductors using a plane-wave basis set, *Comput. Mater. Sci.* **6**, 15 (1996).
- [86] Y. Li, D. Legut, X. Liu, C. Lin, X. Feng, Z. Li, and Q. Zhang, Modulated ferromagnetism and electric polarization induced by surface vacancy in MX_2 monolayers, *J. Phys. Chem. C* **126**, 8817 (2022).
- [87] J. Hong, C.-J. Kang, and J. Kim, Role of electronic correlations in room-temperature ferromagnetism of monolayer MnSe_2 , *Phys. Rev. B* **106**, 195428 (2022).
- [88] J. Jiang, R. Li, and W. Mi, Exchange interactions in the 1T-VSe₂ monolayer and their modulation via electron doping using alkali metal adsorption and the electride substrate, *Mater. Horiz.* **9**, 2785 (2022).
- [89] J.-J. Liao, Y.-Z. Nie, X.-g. Wang, Z.-y. Luo, Q.-l. Xia, R. Xiong, and G.-h. Guo, Spin reorientation and curie temperature promotion in CrI_3 –Bi van der Waals heterostructures, *Phys. Rev. B* **107**, 184403 (2023).
- [90] A. Luo, Z. Song, and G. Xu, Fragile Topological Band in the checkerboard antiferromagnetic monolayer FeSe, *npj Comput. Mater.* **8**, 26 (2022).
- [91] C. T. White, D. H. Robertson, and J. W. Mintmire, Helical and rotational symmetries of nanoscale graphitic tubules, *Phys. Rev. B* **47**, 5485 (1993).
- [92] R. A. Jishi, M. S. Dresselhaus, and G. Dresselhaus, Symmetry properties of chiral carbon nanotubes, *Phys. Rev. B* **47**, 16671 (1993).